Acta Oceanol. Sin., 2020, Vol. 39, No. 3, P. 123–129
https://doi.org/10.1007/s13131-020-1560-x
http://www.hyxb.org.cn
E-mail: hyxbe@263.net

Sensitivity study of the wave-driven current in an Arctic frazil-pancake ice zone

Xueyan Zhang[1], Haijin Dai[1]*, Jun Zhao[1], Heqing Yin[1]

[1] College of Meteorology and Oceanography, National University of Defense Technology, Changsha 410073, China

Received 20 May 2019; accepted 25 June 2019

Abstract

A coupled ocean-ice-wave model is used to study ice-edge jet and eddy genesis during surface gravity wave dissipation in a frazil-pancake ice zone. With observational data from the Beaufort Sea, possible wave dissipation processes are evaluated using sensitivity experiments. As wave energy dissipated, energy was transferred into ice floe through radiation stress. Later, energy was in turn transferred into current through ocean-ice interfacial stress. Since most of the wave energy is dissipated at the ice edge, ice-edge jets, which contained strong horizontal shear, appeared both in the ice zone and the ocean. Meanwhile, the wave propagation direction determines the velocity partition in the along-ice-edge and cross-ice-edge directions, which in turn determines the strength of the along-ice-edge jet and cross-ice-edge velocity. The momentum applied in the along-ice-edge (cross-ice-edge) direction increased (decreased) with larger incident angle, which is favorable condition for producing stronger mesoscale eddies, vice versa. The dissipation rate increases (decreases) with larger (smaller) wavenumber, which enhances (reduces) the jet strength and the strength of the mesoscale eddy. The strong along-ice-edge jet may extend to a deep layer (> 200 m). If the water depth is too shallow (e.g., 80 m), the jet may be largely dampened by bottom drag, and no visible mesoscale eddies are found. The results suggest that the bathymetry and incident wavenumber (magnitude and propagation direction) are important for wave-driven current and mesoscale eddy genesis.

Key words: marginal ice zone, frazil-pancake ice, wave dissipation, ice-edge jet, mesoscale eddy genesis

Citation: Zhang Xueyan, Dai Haijin, Zhao Jun, Yin Heqing. 2020. Sensitivity study of the wave-driven current in an Arctic frazil-pancake ice zone. Acta Oceanologica Sinica, 39(3): 123–129, doi: 10.1007/s13131-020-1560-x

1 Introduction

As an important zone for wave-ice interactions, the marginal ice zone (MIZ) is defined as the transitional zone between the ice-covered sea and the open ocean (Dumont et al., 2011). MIZ widths, which were measured by its ice concentrations from the satellite observations (Strong and Rigor, 2013), usually have a magnitude of 10–100 km. Inside the MIZ, there are multiple sea ice morphological characteristics (Lei et al., 2017). Among them, two important types of young ice (frazil ice and pancake ice) with a diameter of 1–5 m, form in turbulent environments; the behavior (i.e., momentum evolution) of these two types can be well simulated by the mass-loading model (Dai et al., 2019).

Mesoscale eddies are significant features in MIZ, which can be captured by synthetic aperture radar images. Attention has been paid to mesoscale eddies in the MIZ since the 1980s, when the great project "Marginal Ice Zone Experiment (MIZEX)" was carried out to study the physics of mesoscale eddies in the MIZ (Johannessen et al., 1987a). Mesoscale eddies in the MIZ have also been studied via numerical modeling (Hibler, 1979; Williams et al., 2013, 2017; Rampal et al., 2016), mostly based on a 1-layer sea ice model (Røed and O'Brien, 1983; Häkkinen, 1986; Liu et al., 1993). As summarized by results from both observations and numerical simulations, a mesoscale eddy is described as a rotating cylinder with a dimeter of 5–60 km and a maximum orbital velocity of 0.5–0.7 m/s. Johannessen (Johannessen et al., 1987b) also proposed that there are primarily three eddy genesis mechanisms in the MIZ: topographic variation (Gula et al., 2015), nonlinear advection of vorticity (Dai et al., 2017), and barotropic and (or) baroclinic instability of the current (Boccaletti et al., 2007; Manucharyan and Timmermans, 2013; Manucharyan and Thompson, 2017; Zhang et al., 2019).

Dai et al. (2019) demonstrated the eddy genesis mechanism of barotropic instability in wave-ice interactions. This mechanism can be separated into two steps: wave energy dissipates and wave-driven current genesis. When surface gravity waves propagate in the MIZ, reflection and transmission occur simultaneously, which leads to variation in the wavenumber in both the magnitude and the propagation direction. On the other hand, while waves propagate in the MIZ, the wave energy dissipates exponentially with distance from the ice edge (Meylan et al., 2014). Wave dissipated by sea ice is a more crucial process than the wave dissipation due to wave breaking and bottom drag (Uchiyama et al., 2010). The typical e-folding distance is usually considered 1-20 km and is determined by the ice properties and wavenumber (Weber, 1987). However, with the low ice concentration and large wave amplitude in the Southern Ocean, typical swell could propagate over 100 km in the MIZ before the wave energy was completely dissipated by sea ice (Kohout et al., 2014). This is the first step. Liu et al. (1993) suggested that, since both wave energy decay and acceleration of sea ice by wave radiation stress mainly occur at the ice edge, an ice-edge jet (both in the sea ice and current) will be observed. Furthermore, Dai et al.

Foundation item: The National University of Defense Technology under contract No. ZK18-03-29.
*Corresponding author, E-mail: hj_dai@nudt.edu.cn

(2019) found that an ice-edge jet, which shows strong unstable horizontal shear, may help small turbulences grow into mesoscale eddies. This is the second step.

Mesoscale eddies in numerical simulations spatially span tens of kilometers and hundreds of meters at the horizontal and vertical scales, respectively, which is consistent with the observations. A wave-induced ice-edge jet, which leads to mesoscale eddy genesis, is a typical barotropic instability process (Dai et al., 2019). Dai et al. (2019) suggested that a shallower mixed layer and a larger spatial energy decay rate can enhance mesoscale eddy genesis. They also mentioned that both the along-ice-edge jet and the cross-ice-edge current are strengthened by increasing the amplitude of the incident waves. The competition between the along-ice-edge jet and the cross-ice-edge current determines the eddy strength. However, in their work, the wave refractions were always the same, which is unlikely to occur in the realistic simulation.

Wadhams and Holt (1991) demonstrated how the wave refraction varies with different incident angles, wavenumber amplitudes and ice mass variations. The theoretical calculations and observational results were highly consistent in that study. However, they never considered how different wave refractions influenced the ice-edge jet and its instability. In this paper, we attempt to reproduce possible scenarios from the latest observations (Wadhams et al., 2018). We aimed to focus on how different wave refractions influenced the mesoscale eddy genesis beneath the ice zone. Additionally, we discuss possible theoretical results using sensitivity experiments.

This paper is arranged as follows. In Section 2, we introduce the model settings and sensitivity experimental design. In Section 3, we analyze the results of different wave sensitivity experiments. In Section 4, we provide a summary and identify future research topics.

2 Model and experiments

2.1 *Coupled ocean-ice-wave system*

A coupled ocean-ice-wave system composed of an ocean general circulation model (Regional Oceanic Modeling System (ROMS) (Shchepetkin and McWilliams, 2005)), a Wentzel-Kramers-Brillouin wave model (Uchiyama et al., 2010) and a one-layer sea ice model (Dai et al., 2019) is used in this study.

The relevant part of the coupled ocean-ice-wave system is shown as follows (more details can be found in Section 2 of Dai et al. (2019)).

Ocean momentum equation:

$$\frac{\partial \vec{v}}{\partial t} + (\vec{v}\cdot\nabla_\perp)\,\vec{v} + w\frac{\partial \vec{v}}{\partial z} = -\nabla_\perp \Phi - f\vec{z}\times\vec{v} + (1-A_\mathrm{i})\,\overrightarrow{\tau_\mathrm{aw}} - A_\mathrm{i}\overrightarrow{\tau_\mathrm{wi}} + \overrightarrow{F^\mathrm{w}} + \vec{J} - \nabla_\perp \Gamma. \quad (1)$$

Sea ice momentum equation:

$$\rho_\mathrm{i} M_\mathrm{i}\left(\frac{\partial \overrightarrow{v_\mathrm{i}}}{\partial t} + \left(\overrightarrow{v_\mathrm{i}}\cdot\nabla_\perp\right)\overrightarrow{v_\mathrm{i}}\right) = -\rho_\mathrm{i} M_\mathrm{i} f\vec{z}\times\overrightarrow{v_\mathrm{i}} + A_\mathrm{i}\left(\overrightarrow{\tau_\mathrm{ai}} + \overrightarrow{\tau_\mathrm{wi}}\right) + \overrightarrow{F_\mathrm{i}} + \overrightarrow{F_\mathrm{r}}. \quad (2)$$

Wavenumber and wave energy evolution:

$$\frac{\partial \vec{k}}{\partial t} + \overrightarrow{c_\mathrm{g}}\cdot\nabla_\perp\vec{k} = -\vec{k}\nabla_\perp\overrightarrow{\vec{V}} + \frac{k\rho_\mathrm{i}}{2\rho_\mathrm{w}}\frac{\sqrt{gk}}{2(1+B_0 k)^{\frac{3}{2}}}\cdot\nabla_\perp\overrightarrow{M_\mathrm{i}}, \quad (3)$$

$$\frac{\partial \Lambda}{\partial t} + \nabla_\perp\cdot\left(\overrightarrow{c_\mathrm{g}}\Lambda\right) = -\left(1-A_\mathrm{i}\right)\frac{\varepsilon_\mathrm{b}}{\omega_0} + A_\mathrm{i}\alpha c_\mathrm{g}\Lambda. \quad (4)$$

All the symbols are defined in Table 1.

Table 1. Definition of symbols used in Eqs (1)–(4)

Symbol	Name
α	wave energy decay rate due to ice
Λ	wave action
A_i	ice concentration
B_0	parameter defined as $\rho_\mathrm{i}/\rho_0{\cdot}M_\mathrm{i}$
$\overrightarrow{c_\mathrm{g}}$	group velocity vector
ε_b	wave dissipation rate due to breaking
f	Coriolis parameter (0.001 4 s^{-1})
$\overrightarrow{F_\mathrm{i}}$	ice internal stress
$\overrightarrow{F^\mathrm{w}}$	wave-induced nonconservative force
$\overrightarrow{F_\mathrm{r}}$	wave radiation stress
g	gravitational acceleration
$\vec{J}$	vortex forces vector
k	wavenumber amplitude
$\vec{k}$	wavenumber vector
M_i	ice mass over unit area
Φ	potential height
ρ_i	ice density
ρ_w	sea water density
ρ_0	reference density
$\overrightarrow{\tau_\mathrm{ai}}$	wind stresses exerted on the sea ice
$\overrightarrow{\tau_\mathrm{aw}}$	wind stresses exerted on the current
$\overrightarrow{\tau_\mathrm{wi}}$	interfacial stress between the sea water and ice
Γ	Bernoulli head
$\vec{v}$	current velocity vector
$\vec{v_\mathrm{i}}$	sea ice velocity vector
$\overrightarrow{\vec{V}}$	depth-averaged current velocity vector
w	current velocities in the z directions
ω_0	wave intrinsic frequency
$\vec{z}$	unit vector in the vertical direction

The mass-loading model neglects the ice flexure, and usually is used in the frazil-pancake ice simulation. According to the floe breaking parameterization (Dumont et al., 2011), one factor that ice flexure occur is the diameter of the ice floe is larger than half of the wavelength. Since the typical diameter of frazil-pancake ice is 1–5 m, when the wavelength is longer than 10 m, ice flexure in the frazil-pancake ice could be neglected, and not considered here.

2.2 *Experimental setting*

During 30 September to 4 November, 2015, new observations, which were supported by the project "Sea State and Boundary Layer Physics of the Emerging Arctic Ocean", were conducted to observe wave-ice interaction in the frazil-pancake ice in the Beaufort Sea (Thomson et al., 2015; Cheng et al., 2017; Wadhams et al., 2018). For the observations in the experiment of 23–24 October 2015 (Wadhams et al., 2018), frazil-pancake ice dominated the region of 72°–72.75°N, 160°–158°W (discussed with Prof. Wadhams privately), while the ice thickness is approximately to 0.5 m. The surface gravity waves have a wavenumber of 0.012 9–0.968 m^{-1} (wave length is 6.5–487 m) and a significant wave height of 1–2 m in the open ocean. The Global Relief Model data of ETOPO1 (doi:10.7289/V5C8276M) data suggested that the wa-

ter depth in the region of 72°–72.75°N, 160°–158°W, where the observations were carried out, is 50–400 m.

As suggested by the observational data described above and the experiment settings in (Dai et al., 2019), the model is configured for a 200 km×100 km domain with a horizontal resolution of 1 km×1 km. There are 20/40 grid levels in the vertical direction spanning a total depth of 80/400 m. North-south periodic boundaries are employed in this work; however, there are open boundary conditions at the eastern and western boundaries. In the model runs, the reference water density is 1 027.5 kg/m^3. The initial density, temperature and salinity are horizontally uniform and vertically stratified with a buoyancy frequency of N = 0.006 s^{-1} in the mixed layer.

As the effects of wind and large-scale currents are not considered, the ice edge is influenced by incident waves. Thus, the initial velocity fields for both the ice and current are set to zero. No wind stress is applied to this domain. The ice boundary is defined as the boundary where the ice fraction (A_i) is 0.1. At the ice edge, the ice distribution follows a hyperbolic function and is uniform in the along-ice-edge direction.

In the control experiment (designated as Ctrl), the total water depth is 400 m, the incident wave has a wave amplitude of 1.6 m, and the incident wavenumber is 0.034 78 m^{-1} (incident wavelength is 180 m). For the incident wave propagation direction, the incident angle is set to 71.5° (ky/kx=3). The ice thickness is 0.5 m. In the sensitivity experiments, most settings are the same as those in the control experiment; however, we change the following variable. For the incident angle sensitivity, we set the incident angle to 78.5° (ky/kx=5, designated as 5Tan) and 60° (ky/kx= 1.7, designated as 1.7Tan). For bathymetry sensitivity, we set the water depth to 80 m (designated as 80H). For the wavenumber sensitivity, we set the incident wavenumber to 0.069 56 m^{-1} (incident wavelength of 90 m, designated as Hfrq) and 0.017 39 m^{-1} (incident wavelength of 360 m, designated as Lfrq). For convenience, we summarize each sensitivity experiment in Table 2. All cases are integrated for 54 days until reaching equilibrium. In the next section, we use Ctrl, 5Tan, 1.7Tan, 80H, Hfrq and Lfrq to represent the experiment names.

Table 2. Parameters used for the sensitivity experiments

Name	Water depth/m	Wavelength/m	Incident angle/(°)
Ctrl	400	180	71.5
5Tan	400	180	78.5
1.7Tan	400	180	60
Hfrq	400	90	71.5
Lfrq	400	360	71.5
80H	80	180	71.5

Note: Tan means the incident angle is arctan, H the water depth, and frq the wave frequency (high (H) or low (L)).

3 Results and analysis

3.1 *Wave energy dissipation and ice-edge jet genesis*

As waves propagate into the ice zone, the wave energy is consumed by the ice floe. The dissipated wave energy accelerates the sea ice in the same direction as the wave propagation via wave radiation stress. In the cross-ice-edge direction, strong ice internal stress is produced by ice mass gradient and velocity shear (Fig. 1a). The ice internal stress prevents ice from convergence. In the along-ice-edge direction, the momentum is transformed from the sea ice to the current through the ocean-ice interfacial stress, which makes along-ice-edge jets appeared both in the ice zone and in the ocean (Fig. 1b). Both the along-ice-edge velocity and the cross-ice-edge velocity decrease with depth, which indicates that most of the momentum is kept in the upper layers. The along-ice-edge jet extends more than 200 m in the vertical direction, and the velocity is much stronger in the along-ice-edge direction than in the cross-ice-edge direction (Figs 1c, d). On the other hand, the current velocity decreases with depth. As a result, we define the jet strength as the maximum of surface velocity in the along-ice-edge direction.

The strength of the along-ice-edge jet is determined by the amount of the input momentum and the momentum partition in the along-ice-edge direction and the cross-ice-edge direction. When the incident angle increases, the ice mass gradient along the wave propagation direction decreases, which influences wave attenuation. When the incident angles are 60° (1.7Tan), 71.5° (Ctrl), and 78.5° (5Tan), the energy dissipation e-folding distances are 4, 9.7, and 21 km, respectively. As the wave energy dissipated mainly in the cross-ice-edge direction (ice concentration increases greatly in the cross-ice-edge direction at the ice-edge), the e-folding distance should nearly be equal in the cross-ice-edge direction. When the incident angle increases, the e-folding distance in the along-ice-edge direction largely enhances. The dissipated wave energy spreads across a wider region with a longer e-folding distance. Thus, the jet strength in the Ctrl experiment (0.28 m/s, Fig. 2 blue column) is larger than that in the 5Tan experiment (0.26 m/s). On the other hand, a larger incident angle results in more (less) momentum partitioned in the along (cross)-ice-edge direction and produces a stronger jet strength. Thus, the jet strength in the 1.7Tan experiment (0.16 m/s) is smaller than that in the Ctrl experiment. In the cross-ice-edge direction (Fig. 2 red column), the velocity is mainly determined by the momentum partition, which indicates that a larger incident angle produces a smaller cross-ice-edge flow. The cross-ice-edge velocities on day 3 are 0.12 m/s, 0.09 m/s, and 0.15 m/s in the Ctrl, 5Tan, and 1.7Tan experiments, respectively.

The wavenumber determines the dissipation rate, and a larger wavenumber leads to a smaller e-folding distance (Weber, 1987), which in turn produces a stronger jet (Dai et al., 2019). As a result, the along-ice-edge (cross-ice-edge) velocities are 0.34 (0.1) m/s and 0.21 (0.087) m/s in the Hfrq and Lfrq experiments, respectively. As the current momentum equals the water mass times the velocity, most of the current momentum is in the upper layer (approximately 200 m depth). When the water depth decreases, we consider the water mass to be smaller. As a result, the current velocity (especially at the surface) is enhanced based on the conservation of momentum. The jet strength in the 80H experiment (0.33 m/s) is larger than that in the Ctrl experiment. The horizontal shear of the current (Fig. 2b green column) is mostly determined by the jet strength, and a smaller jet strength produces smaller current shear.

3.2 *Mesoscale eddy genesis*

Due to the strong horizontal shear in the along-ice-edge jet, energy is transferred from the mean flow to the turbulence field (Dai et al., 2019). Significant amount of turbulent kinetic energy (TKE) appears on day 20 in the upper 50 m of the Ctrl experiment (Fig. 3a). As time passes, the TKE increases and is transported to lower layers, with a maximum value at the layer at 100 m. In the 5Tan experiment, the TKE (Fig. 3b) appears earlier and has a larger maximum value than the TKE in the other experiments. In the 1.7Tan experiments, there is no significant amount of TKE (Fig. 3c). In the Hfrq experiment, the TKE appears (Fig. 3d) earlier and has a larger maximum value than the TKE in the Ctrl ex-

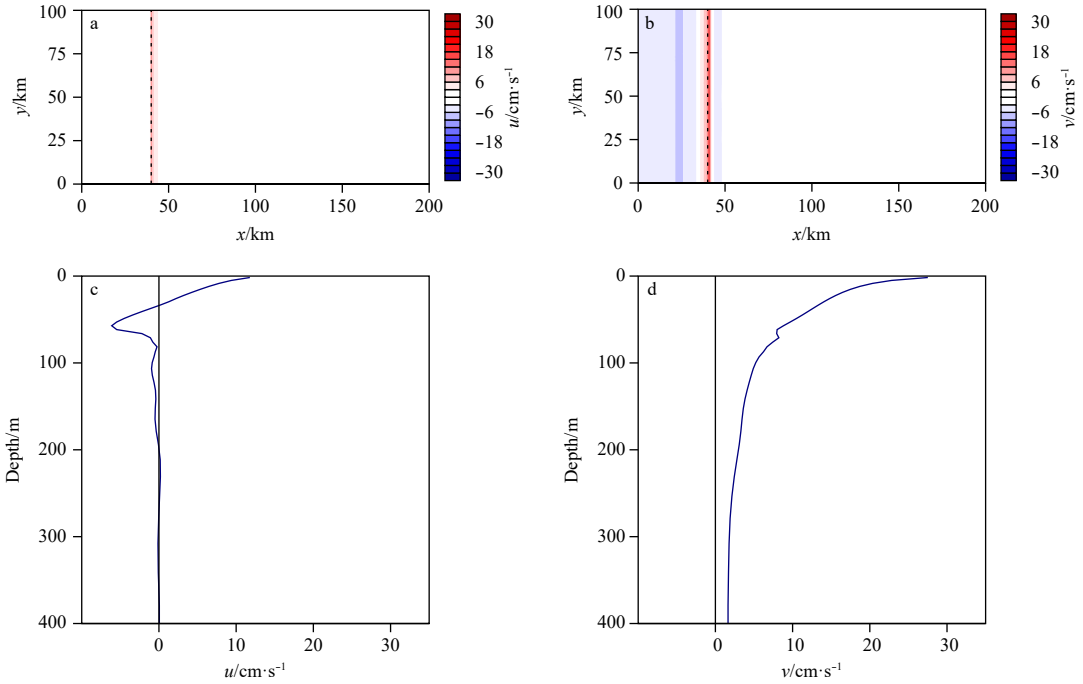

Fig. 1. The distribution of the surface current velocity in the cross-ice-edge direction (a) and along-ice-edge direction (b) on day 3 in Ctrl. The black dotted line indicates the location of the ice boundary. The vertical profile of the cross-ice-edge velocity (c) and along-ice-edge velocity (d) in the jet zone.

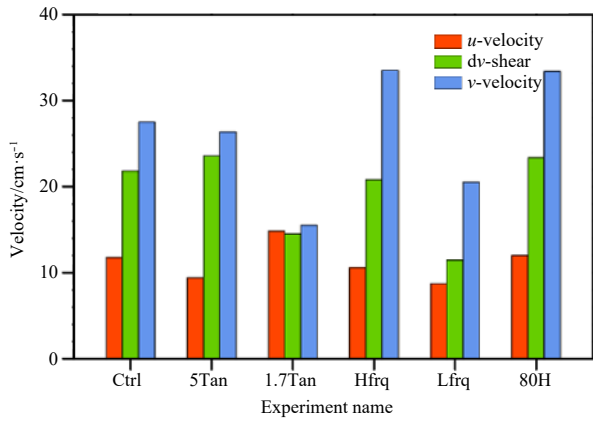

Fig. 2. Maximum value of the along-ice-edge velocity (v, blue column), the cross-ice-edge velocity (u, red column) and the horizontal shear (dv, green column) on day 3 in each sensitivity experiment.

periment. In the Lfrq experiment, the TKE (Fig. 3e) appears later and has a smaller maximum value than the TKE in the Ctrl experiment. In the 80H experiment, there is no significant amount of TKE (Fig. 3f).

Several factors (jet strength (v), the horizontal shear (dv) and velocity in the cross-ice-edge direction (u)) have been proposed to determine the strength of the TKE (Dai et al., 2019; we are mainly concerned with the eddy genesis in the ice zone; thus, we only consider the velocity shear on the ice zone side of the jet).

From the perspective of energy, mesoscale eddy genesis is considered as kinetic energy transferred from mean flow to the turbulence (barotropic instability). As the mean flow is uniformed in the along-ice-edge direction at the beginning, mean kinetic energy (MKE) is approximately proportional to the square of the jet strength. As the energy transferred from mean flow to the turbulence due to the production term $\left(\overline{u'v'}\frac{\mathrm{d}\bar{v}}{\mathrm{d}x}\right)$, the horizontal shear can be viewed as the energy transfer efficiency, which determines how fast the energy is transferred from mean flow to the turbulence. On the other hand, the jet always follows the ice-edge, where the wave energy dissipation mainly occurs, velocity in the cross-ice-edge direction determine how long the jet stay or local current absorbing the unstable energy (ice velocity is nearly equal to the sea surface velocity).

To better understand this process, budget equation for TKE $\left(q=\frac{1}{2}\overline{u_i'u_i'}\right)$ is presented as follows (the derivation was presented in Dai et al. 2019):

$$\frac{\partial q}{\partial t}+\overline{u_i}\frac{\partial q}{\partial x_i}+\overline{u_i'u_j'}\frac{\partial \overline{u_i}}{\partial x_i}+\frac{1}{2}\overline{\frac{\partial u_j'u_j'u_i'}{\partial x_i}}$$
$$=-\frac{1}{\rho_0}\overline{\frac{\partial u_i'P'}{\partial x_i}}+\overline{w'b'}+\nu\frac{\partial^2 q}{\partial x_i^2}-\nu\overline{\frac{\partial u_i'}{\partial x_j}\frac{\partial u_i'}{\partial x_j}}, \quad (5)$$

where u_i represents the current velocity in x ($u=u_1$, i=1), y ($v=u_2$, i=2) and z ($w=u_3$, i=3) direction; b represents buoyancy; $\overline{(\,)}$ indicates averaged in the along-ice-edge direction, and $(\,)'$ indicates a perturbation. Thus, we have $b=[b](z,t)+\bar{b}(x,z,t)+b'(x,y,z,t)$ and $u_i=\overline{u_i}+u_i'$.[] indicates averaged in both the x and y directions. P indicates pressure in the water, ν is molecular viscous coefficient, ρ_0 indicates reference density.

Sometimes, the period of the local current absorbing the unstable energy dominates the TKE genesis. Although the horizontal shear is nearly the same in the Ctrl and 5Tan experiments, the smaller cross-ice-edge velocity in the 5Tan experiment than in the Ctrl experiment allows the local current to absorb more un-

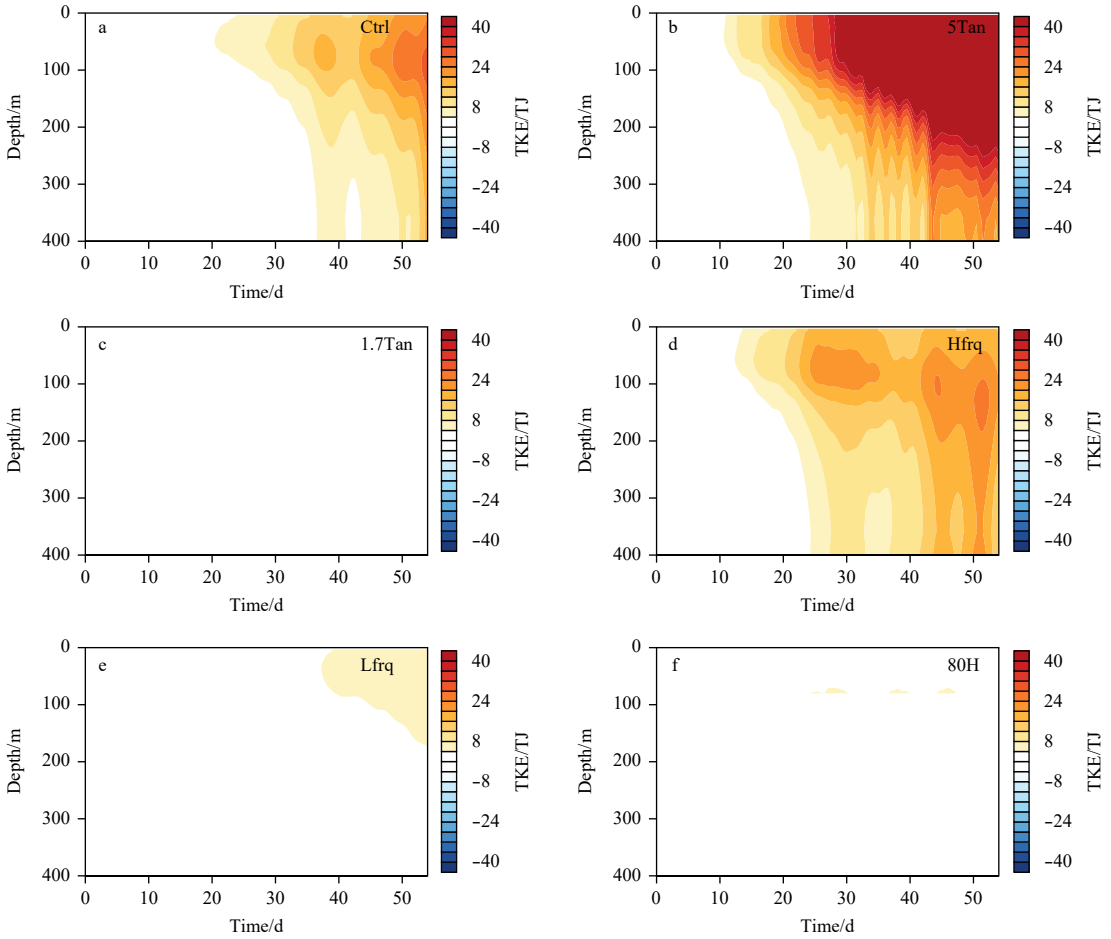

Fig. 3. Evolution of the turbulent kinetic energy at each layer in Ctrl (a), 5Tan (b), 1.7Tan (c), Hfrq (d), Lfrq (e), and 80H (f).

stable energy, which results in a larger TKE (32.79 TJ) in the former than in latter (8.63 TJ) (Fig. 4 red column). The faster the cross-ice-edge current is, the weaker the TKE will be. If both the horizontal shear and period conditions are inadequate for eddy genesis (1.7Tan), the situation is not conducive for producing significant amount of TKE. Additionally, horizontal shear may sometimes dominate eddy genesis. A larger incident wavenumber leads to a larger wave dissipation rate in the Hfrq experiment, which in turn increases the jet strength. As a result, the TKE in the Hfrq experiment (8.77 TJ) is greater than that in the Ctrl experiment. In contrast, in the Lfrq experiment, as the incident wavenumber decreases, the wave dissipation rate becomes much weaker, which in turn produces a smaller jet strength and horizontal shear. As a result, the TKE (2.27 TJ) in the Lfrq experiment is smaller than that in the Ctrl experiment. A smaller mass increases the surface current velocity (80H); however, a faster current in the bottom layer (in the supplementary material) may lead to increased energy loss via bottom drag. As a result, the TKE is very small. This result also suggests that a larger TKE corresponds to increased turbulent available potential energy (TAPE) (Fig. 4 green column) and total turbulent energy (Fig. 4 blue column).

On both sides of the jet zone, there is mesoscale eddy genesis. We can see anticyclonic eddies on the side of ice zone from vorticity (Fig. 5 shading) and velocity (Fig. 5 vector), in contrast, cyclonic eddies on the other side. The TKE determines the horizontal scale of the mesoscale eddies. When the TKE nearly reached

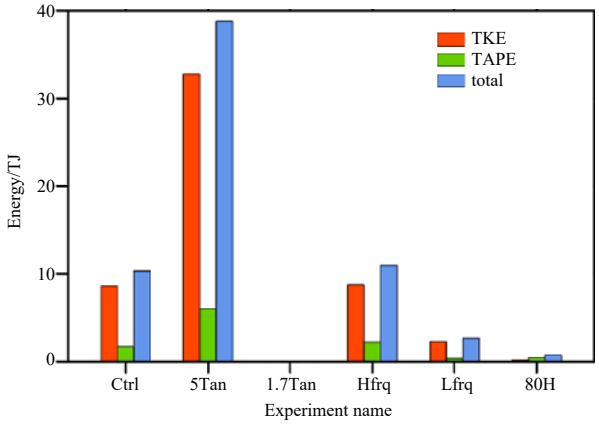

Fig. 4. The maximum of turbulent kinetic energy (red column), turbulent available potential energy (green column), and total turbulent energy (blue column) during 54 days in each sensitivity experiment.

the equilibrium in the last few days, so was the eddy size. Based on the discussion above, in the experiments of Ctrl, the diameters of the primary mesoscale eddy (Fig. 5a, x=105 km) is smaller than that in the experiment of 5Tan (Fig. 5b, x=95 km). No significant mesoscale eddy is observed in the experiment of 1.7Tan because of negligible TKE. The diameter of the primary meso-

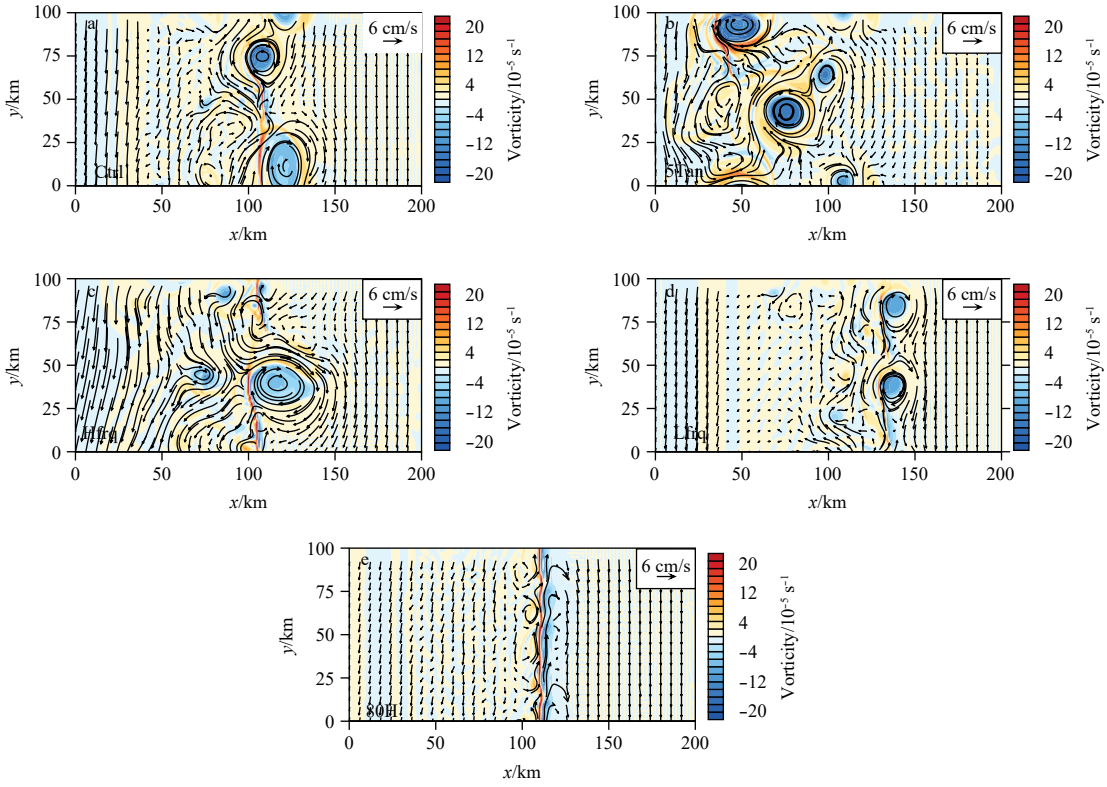

Fig. 5. The vorticity at the sea surface in Ctrl (a), 5Tan (b), Hfrq (c), Lfrq (d), and 80H (e) on Day 54.

scale eddy in the experiment of Hfrq (Lfrq) is larger (smaller) than that in the experiment of Ctrl (Figs 5c, d), while no significant mesoscale eddy is observed in the experiment of 80H as the TKE is quite small (Fig. 5e).

4 Summary and discussion

In this study, the wave-ice-current interactions in an MIZ were investigated using a coupled ocean-ice-wave model. We tested possible wave dissipation processes in a frazil-pancake ice zone. As discussed in Dai et al. (2019), these wave-ice interactions can be described as follows: when surface gravity waves propagate into the ice zone, both wave refraction and wave reflection occur at the ice boundary. As the waves penetrate into the ice zone, the wave energy is quickly dissipated by the sea ice. The dissipated energy accelerates the ice floe through radiation stress. Both the wave dissipation and ice floe acceleration occur mainly near the ice boundary, which is the location of an ice-edge jet with a strong horizontal shear. In addition, possible submesoscale turbulence accumulates and eventually leads to mesoscale eddy genesis.

A larger incident angle leads to increased current momentum in the along-ice-edge direction and decreased momentum in the cross-ice-edge direction, both of which are good for unstable energy growth. Wavenumber is also important during wave dissipation; a larger wavenumber results in a stronger wave dissipation rate. A shallower water depth (in the experiment, 80 m) may increase the current velocity through the conservation of momentum. However, this shallower water depth also increases the bottom drag and consumes more energy. As a result, no visible mesoscale eddy could be found, even when the case was integrated for a long period. Ultimately, we conclude that the bathymetry and incident wavenumber (both the magnitude and propagation direction) are important during ice-edge jet and mesoscale eddy genesis.

The purpose of this paper is to reproduce possible scenarios in the Beaufort Sea and demonstrate the wave-driven current and subsequent mesoscale eddies in frazil-pancake ice. The problem remains somewhat idealized, and the wave-ice interaction is isolated from other polar physical processes, such as wind stress forcing, sea ice thermodynamics, evaporation, precipitation, solar radiation and air-sea heat fluxes.

If we attempt to study the wave-ice interactions for a larger or thicker ice floe, recent observations revealed that ice floe size and ice thickness, which are relevant to ridges among the ice floes, should be considered (Wang et al., 2016; Horvat et al., 2016; Hwang et al., 2017). Besides, the ice dissipation model must be revised since the ice floe diameter can determine the ice dissipation rate, and the wave energy may be consumed by ice flexure. Furthermore, the Young's modulus parameter can no longer be neglected, and the thin plate equation, as well as the wave dispersion relation, will be more complicated.

However, in this study, we made progress in two main areas. First, we discussed the wavenumber variation that may lead to different results during the wave-driven current process. Second, because the energy was largely consumed by bottom drag during the sensitivity experiment, we determined that the barotropic instability mechanism may not work for a shallow water depth. Based on our previous studies, the eddy genesis mechanisms of baroclinic instability and nonlinear advection perform well in shallow water. The question remains: which factor is more crucial? We will study this topic further in our future work.

Acknowledgements

We are grateful to Junhong Liang for useful suggestions. We

are also grateful to A F Shchepetkin and Y Uchiyama for sharing the code of ocean model and wave model.

References

Boccaletti G, Ferrari R, Fox-Kemper B. 2007. Mixed layer instabilities and restratification. Journal of Physical Oceanography, 37(9): 2228–2250, doi: 10.1175/JPO3101.1

Cheng Sukun, Rogers W E, Thomson J, et al. 2017. Calibrating a viscoelastic sea ice model for wave propagation in the Arctic fall marginal ice zone. Journal of Geophysical Research: Oceans, 122(11): 8770–8793, doi: 10.1002/2017JC013275

Dai Haijin, Cui Jian, Yu Jingping. 2017. Revisiting mesoscale eddy genesis mechanism of nonlinear advection in a marginal ice zone. Acta Oceanologica Sinica, 36: 14–20

Dai Haijin, McWilliams J C, Liang Junhong. 2019. Wave-driven mesoscale currents in a marginal ice zone. Ocean Modelling, 134: 1–17, doi: 10.1016/j.ocemod.2018.11.006

Dumont D, Kohout A, Bertino L. 2011. A wave-based model for the marginal ice zone including a floe breaking parameterization. Journal of Geophysical Research: Oceans, 116(C4): C04001

Gula J, Molemaker M J, McWilliams J C. 2015. Topographic vorticity generation, submesoscale instability and vortex street formation in the Gulf Stream. Geophysical Research Letters, 42(10): 4054–4062, doi: 10.1002/2015GL063731

Häkkinen S. 1986. Coupled ice-ocean dynamics in the marginal ice zones: upwelling/downwelling and eddy generation. Journal of Geophysical Research: Oceans, 91(C1): 819–832, doi: 10.1029/JC091iC01p00819

Hibler W D III. 1979. A dynamic thermodynamic sea ice model. Journal of Physical Oceanography, 9(4): 815–846, doi: 10.1175/1520-0485(1979)009<0815:ADTSIM>2.0.CO;2

Horvat C, Tziperman E, Campin J M. 2016. Interaction of sea ice floe size, ocean eddies, and sea ice melting. Geophysical Research Letters, 43(15): 8083–8090, doi: 10.1002/2016GL069742

Hwang B, Wilkinson J, Maksym T, et al. 2017. Winter-to-summer transition of Arctic sea ice breakup and floe size distribution in the Beaufort Sea. Elem Sci Anth, 5: 40, doi: 10.1525/elementa.232

Johannessen J A, Johannessen O M, Svendsen E, et al. 1987a. Mesoscale eddies in the Fram Strait marginal ice zone during the 1983 and 1984 Marginal Ice Zone Experiments. Journal of Geophysical Research, 92(C7): 6754–6772, doi: 10.1029/JC092iC07p06754

Johannessen O M, Johannessen J A, Svendsen E, et al. 1987b. Ice-edge eddies in the Fram Strait marginal ice zone. Science, 236(4800): 427–429, doi: 10.1126/science.236.4800.427

Kohout A L, Williams M J M, Dean S M, et al. 2014. Storm-induced sea-ice breakup and the implications for ice extent. Nature, 509(7502): 604–607, doi: 10.1038/nature13262

Lei Ruibo, Tian-Kunze X, Li Bingrui, et al. 2017. Characterization of summer Arctic sea ice morphology in the 135°-175°W sector using multi-scale methods. Cold Regions Science and Technology, 133: 108–120, doi: 10.1016/j.coldregions.2016.10.009

Liu A K, Häkkinen S, Peng C Y. 1993. Wave effects on ocean-ice interaction in the marginal ice zone. Journal of Geophysical Research, 98(C6): 10025–10036, doi: 10.1029/93JC00653

Manucharyan G E, Thompson A F. 2017. Submesoscale sea ice-ocean interactions in marginal ice zones. Journal of Geophysical Research: Oceans, 122(12): 9455–9475, doi: 10.1002/2017JC012895

Manucharyan G E, Timmermans M L. 2013. Generation and separation of mesoscale eddies from surface ocean fronts. Journal of Physical Oceanography, 43(12): 2545–2562, doi: 10.1175/JPO-D-13-094.1

Meylan M H, Bennetts L G, Kohout A L. 2014. In situ measurements and analysis of ocean waves in the Antarctic marginal ice zone. Geophysical Research Letters, 41(14): 5046–5051, doi: 10.1002/2014GL060809

Rampal P, Bouillon S, Ólason E, et al. 2016. neXtSIM: a new Lagrangian sea ice model. The Cryosphere, 10(3): 1055–1073, doi: 10.5194/tc-10-1055-2016

Røed L P, O'Brien J J. 1983. A coupled ice-ocean model of upwelling in the marginal ice zone. Journal of Geophysical Research, 88(C5): 2863–2872, doi: 10.1029/JC088iC05p02863

Shchepetkin A F, McWilliams J C. 2005. The regional oceanic modeling system (ROMS): a split-explicit, free-surface, topography-following-coordinate oceanic model. Ocean Modelling, 9(4): 347–404, doi: 10.1016/j.ocemod.2004.08.002

Strong C, Rigor I G. 2013. Arctic marginal ice zone trending wider in summer and narrower in winter. Geophysical Research Letters, 40(18): 4864–4868, doi: 10.1002/grl.50928

Thomson J. 2015. ONR sea state DRI cruise report. Washington, DC: Office of Naval Research Sea State Initiative, Applied Physics Lab, University of Washington

Uchiyama Y, McWilliams J C, Shchepetkin A F. 2010. Wave-current interaction in an oceanic circulation model with a vortex-force formalism: Application to the surf zone. Ocean Modelling, 34(1–2): 16–35, doi: 10.1016/j.ocemod.2010.04.002

Wadhams P, Aulicino G, Parmiggiani F, et al. 2018. Pancake ice thickness mapping in the Beaufort Sea from wave dispersion observed in SAR imagery. Journal of Geophysical Research: Oceans, 123(3): 2213–2237, doi: 10.1002/2017JC013003

Wadhams P, Holt B. 1991. Waves in frazil and pancake ice and their detection in Seasat synthetic aperture radar imagery. Journal of Geophysical Research: Oceans, 96(C5): 8835–8852, doi: 10.1029/91JC00457

Wang Yu, Holt B, Erick Rogers W, et al. 2016. Wind and wave influences on sea ice floe size and leads in the Beaufort and Chukchi Seas during the summer-fall transition 2014. Journal of Geophysical Research: Oceans, 121(2): 1502–1525, doi: 10.1002/2015JC011349

Weber J E. 1987. Wave attenuation and wave drift in the marginal ice zone. Journal of Physical Oceanography, 17(12): 2351–2361, doi: 10.1175/1520-0485(1987)017<2351:WAAWDI>2.0.CO;2

Williams T D, Bennetts L G, Squire V A, et al. 2013. Wave-ice interactions in the marginal ice zone. Part 2: Numerical implementation and sensitivity studies along 1D transects of the ocean surface. Ocean Modelling, 71: 92–101

Williams T D, Rampal P, Bouillon S. 2017. Wave-ice interactions in the neXtSIM sea-ice model. The Cryosphere, 11(5): 2117–2135, doi: 10.5194/tc-11-2117-2017

Zhang Xueyan, Dai Haijin, Zhao Jun, et al. 2019. Generation mechanism of an observed submesoscale eddy in the Chukchi Sea. Deep Sea Research Part I: Oceanographic Research Papers, 148: 80–87, doi: 10.1016/j.dsr.2019.04.015